Fast Localization and Segmentation of Optic Disk in Retinal Images Using Directional Matched Filtering and Level Sets

H. Yu, *Member, IEEE*, E. S. Barriga, *Member, IEEE*, C. Agurto, *Student Member, IEEE*, S. Echegaray, *Student Member, IEEE*, M. S. Pattichis, *Senior Member, IEEE*, W. Bauman, and P. Soliz, *Member, IEEE*

***Abstract*—The optic disk (OD) center and margin are typically requisite landmarks in establishing a frame of reference for classifying retinal and optic nerve pathology. Reliable and efficient OD localization and segmentation are important tasks in automatic eye disease screening. This paper presents a new, fast, and fully automatic OD localization and segmentation algorithm developed for retinal disease screening. First, OD location candidates are identified using template matching. The template is designed to adapt to different image resolutions. Then, vessel characteristics (patterns) on the OD are used to determine OD location. Initialized by the detected OD center and estimated OD radius, a fast, hybrid level-set model, which combines region and local gradient information, is applied to the segmentation of the disk boundary. Morphological filtering is used to remove blood vessels and bright regions other than the OD that affect segmentation in the peripapillary region. Optimization of the model parameters and their effect on the model performance are considered. Evaluation was based on 1200 images from the publicly available MESSIDOR database. The OD location methodology succeeded in 1189 out of 1200 images (99% success). The average mean absolute distance between the segmented boundary and the reference standard is 10% of the estimated OD radius for all image sizes. Its efficiency, robustness, and accuracy make the OD localization and segmentation scheme described herein suitable for automatic retinal disease screening in a variety of clinical settings.**

***Index Terms*—Automatic eye disease screening, level set segmentation, optic disk (OD) localization, parameter optimization.**

I. Introduction

AUTOMATED analysis algorithms provide an objective, accurate, and efficient solution to the high demand of screening for eye diseases such as diabetic retinopathy (DR). DR is a retinal disease caused by complications of diabetes mellitus, which can eventually lead to blindness. By detecting eye disease early through automated screening algorithms, treatment would become more effective and significant savings in health care costs could be realized.

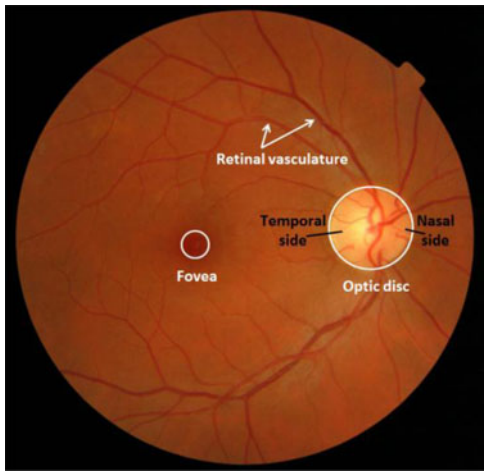

Fig. 1. Retinal image landmarks.

One of the first requirements for automatic eye screening system is the localization of anatomical landmarks such as the optic disk (OD), fovea, and retinal vasculature (see Fig. 1). The OD is the region of the posterior pole where the vasculature and retinal nerve axons enter and leave the eye. The OD in a healthy retinal image usually appears as a bright yellowish and elliptical object marked by surface vessels; its bright appearance is in contrast to the darker surrounding retinal tissue. The absence of the pigmented epithelium in this zone is responsible for the yellowish color of the OD in the digital fundus image.

The appearance of the OD, as well as the retina, may vary significantly. The natural concave shape of the retina, in addition to the large individual variation in the melanin concentration of the retinal pigment epithelium layer of the retina, is responsible for different levels of reflected illumination from the fundus. The presence of pathologic changes occurring at the site of the OD, such as neovascularization from DR or changes to the physiologic cup due to glaucoma, can also affect its appearance dramatically. Other anomalies, including myopic crescents, peripapillary atrophy (PPA), and myelinated nerve fibers distort the size, shape, and brightness of the OD. Image quality can also affect the appearance of the OD. A retinal image may be

Manuscript received June 29, 2011; revised March 23, 2012; accepted April 28, 2012. Date of publication May 10, 2012; date of current version July 5, 2012. This work was supported by the National Institutes of Health under Grant EY018280 and Grant EY020015.

H. Yu, E. S. Barriga, and P. Soliz are with the VisionQuest Biomedical, Albuquerque, NM 87106 USA (e-mail: honggang@ece.unm.edu; sbarriga@visionquest-bio.com; psoliz@visionquest-bio.com).

C. Agurto and M. S. Pattichis are with the Department of Electrical and Computer Engineering, University of New Mexico, Albuquerque, NM 87131 USA (e-mail: capaagri@unm.edu; pattichis@ece.unm.edu).

S. Echegaray is with the Department of Electrical Engineering, Stanford University, Palo Alto, CA 94305-2004 USA (e-mail: sechegaray@gmail.com).

W. Bauman is with the Retina Institute of South Texas, San Antonio, TX 78209 USA (e-mail: bauman1@sbcglobal.net).

Color versions of one or more of the figures in this paper are available online at http://ieeexplore.ieee.org.

Digital Object Identifier 10.1109/TITB.2012.2198668

unevenly illuminated or poorly focused, resulting in a less distinct and blurred OD. Also, the temporal side of the OD is usually brighter than the nasal side, especially in macula-centered photographs. Images exhibiting large variations in the appearance of the OD are shown in the first column of Fig. 4. In the development of an automatic OD localization and segmentation methodology, it is important to consider all major OD variations.

OD detection is the first and necessary step for automated DR screening. Since the OD shares pixel intensity and color characteristics with bright lesions such as hard exudates, DR screening algorithms must avoid including OD information that mask lesion features [1]–[3]. Additionally, the OD is important in localization of the fovea/macula, the center of the retina, where signs of sight-threatening disease may appear. We also note that OD margin segmentation is essential to the detection of abnormalities associated with the OD, e.g., neovascularization on the disk (NVD), papilledema, and glaucoma [4], [5]. Glaucoma can be characterized by gradual cupping of the optic nerve head. The size of the OD and the shape of the boundary are quantitative metrics used for glaucoma diagnosis and progression monitoring. The disk margin is used to measure cup-to-disk vertical ratio, cup-to-disk area ratio, etc. We do not consider these OD pathologies further in this paper.

A. OD Detection

Reliable OD detection is surprisingly difficult, due to the variability in its appearance and confounding bright pathologies. Many approaches have been developed in order to detect the OD. Here some of the most common methods are summarized; a more detailed review of them can be found in [6] and [7]. In previous investigations, intensity and shape have been the main features used to locate the position of the OD. Methods based on intensity variance [8], principal component analysis and model-based method [9], [10], template matching [11], pyramidal decomposition with the Hausdorff-based template matching [12], 1-D projection of image features to obtain fast localization [13], and linear operators [14] have been reported in the literature. Other approaches exploit the location and orientation of vasculature in the retinal image [7], [15]–[18]. Fuzzy convergence of blood vessels to locate the center of OD was used in [19]. An approach to localize the OD by fitting a parametric geometrical model to the main vessels is proposed in [20]. The use of the vasculature network can improve OD localization reliability, especially when the OD is not visible due to advanced retinal pathologies within the image. However, the accurate segmentation of the vascular tree in the entire image to detect the OD is a complex and time-consuming task, taking up to several minutes [7], [15], [16], [20]. The performance of vasculature segmentation can be affected by bright lesions, red lesions, and the OD contour. Any misclassification may degrade the performance of subsequent OD detection.

The motivation behind the proposed methodology is to develop a fast, efficient, and robust algorithm for OD localization as a prerequisite step in eye disease screening. The proposed approach uses template matching with adaptive template size design in CIELab lightness image to select OD candidates. Further identification of the OD location is implemented by using properties of vessels on the OD surface. Instead of segmenting the whole vascular network in the entire image, a simple and efficient directional matched filter in the green channel is applied to OD candidates to obtain the vessel location and orientation within the OD region. In this way, we achieve robust OD localization with a short processing time solving the problems encountered by previous techniques described in the literature.

B. OD Segmentation

Active contours have been one of the most promising approaches for OD segmentation. Mendels *et al.* [21] explored use of a morphological operator followed by the gradient vector flow (GVF) active contour to segment the disk with an interactively initialized curve, which is set close to the true contour of the OD. Their technique was tested on a set of nine retinal images, but no quantitative evaluation was presented. Osareh *et al.* [11] proposed intensity template matching to initialize the deformable contour. They then used color morphological processing to obtain a more homogeneous inner disk area, which increased the accuracy of the GVF active contour segmentation. An overall accuracy of 90.32% was reported in comparison to the reference standard of a clinical ophthalmologist on 75 images. Lowell *et al.* [22] used a global elliptical parametric model combined with a local variable edge-strength-dependent stiffness model to fit the contour of the OD. The algorithm was evaluated on 90 images, achieving "excellent-fair" performance in 83% of the cases. The performance of this method is sensitive to the curve initialization. Li and Chutatape [23] proposed a modified active shape model to segment the OD. The algorithm successfully detected the OD boundary in 33 of 35 images. For their model, we note that significant effort is needed to set up the point correspondences using an appropriate training set. Another deformable model, proposed by Xu *et al.* [24] was enforced by additional constraints of knowledge-based clustering and smoothing update to reduce false deformation in disk segmentation. Their method achieved a 94% success rate on 100 images. The segmentation failed when the images had pathological regions larger and brighter than the OD. Joshi *et al* [5] attempted to segment the OD in the presence of atrophy. They improved region-based active contour model [25] by using local red channel intensity and two texture feature spaces in the neighborhood of the interested pixels. Quantitative evaluation was made on 138 retinal images with 30° field of view (FOV). Their model is based on the assumption that textural features obtained from an OD surrounded by atrophy are different from the ones obtained from a healthy OD. However, these feature differences might be too subtle due to the heterogeneity inside OD, especially after morphology vessel removal. This method is computationally expensive, as two local textural features are used.

Recently, Aquino *et al.* [26] presented a fast OD boundary segmentation technique and tested it on 1200 images in the MESSIDOR database. They applied the circular Hough transform, which was also used by Chrastek *et al.* [27]. The segmentation was performed in parallel, using both the red and green

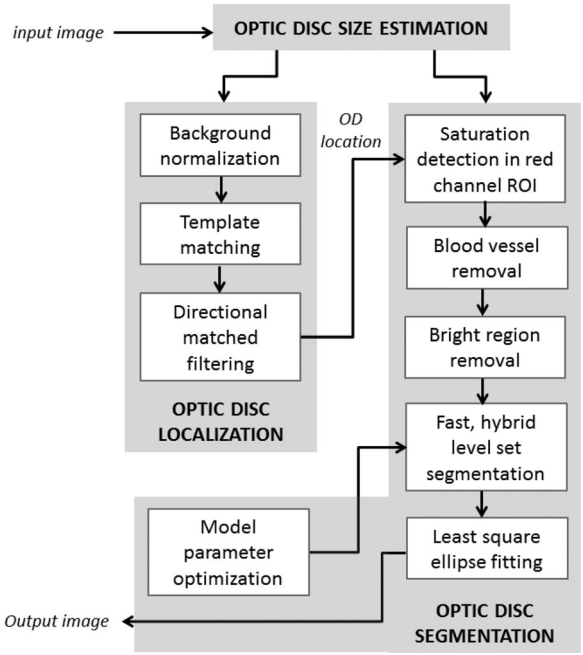

Fig. 2. OD localization and segmentation methodology block diagram.

channel of down-sampled images. The color channel with the higher score in the circular Hough transform on the Prewitt edge map was selected for OD boundary segmentation. An overlapping area of 86% with the reference standard was achieved. However, noise and spurious edge points due to heterogeneity in OD region can potentially give incorrect peak locations at parameter space in the Hough transform.

Our OD segmentation algorithm was developed using a fast, hybrid level set model, which will be shown to provide more accurate delineation of the disk boundary than the Hough transform, and was validated on 1200 images from the MESSIDOR database. The algorithm is insensitive to curve initialization. The vessels and bright region distractors in the peripapillary region are removed using alternating sequential filtering (ASF) and morphological reconstruction. The fast, hybrid level set model deforms the evolving curve based on the region and local edge information, which performs well on the blurred disk margin. The threshold value is adaptively computed using image-dependent statistics. Optimization of model parameters ensures the best segmentation performance.

The paper is organized as follows. In Section II, we present the methodology for OD localization and boundary segmentation. The results of the tests on the images of the MESSIDOR database are presented in Section III. Comparison with results from applying the Hough transform-based method [25] to the same database can be found in Section IV. Finally, Section V is devoted to the conclusions of this study.

II. Methodology

The OD localization and segmentation methodology presented herein can be schematically described by the block diagram in Fig. 2. The method consists of three main processing phases: 1) OD size estimation adaptive to different image resolution, 2) OD localization, for determining the location of the disk center; and 3) OD boundary segmentation. These phases are further subdivided into several steps and described as follows.

A. OD Size Estimation

An important parameter that needs to be determined in our OD detection and segmentation algorithm is the size of the OD. Most of the research works in the literature estimate this parameter by averaging OD diameters using a subset of images [11], [22]. This approach is tedious and impractical for large datasets.

Using the FOV of the camera and image resolution, we formulated a new approach to calculate the OD size. The MESSIDOR database images were acquired with a 45° FOV, which results in a retinal area of 124.8 mm^2 [28].

If the number of pixels in the FOV is N_{FOV}, the image footprint is computed as

$$f_{\text{img}} = \frac{A_{\text{FOV}}}{N_{\text{FOV}}} \tag{1}$$

where A_{FOV} is the imaging area of the specific FOV, in this case, $A_{\text{FOV}} = 124.8\ \text{mm}^2$.

We calculate the OD radius in pixels $r_{\text{OD\_img}}$ based on the diameter of the average human optic nerve head, which has been reported to be approximately 1.85 mm [29]

$$r_{\text{OD\_img}} = \sqrt{\frac{(A_{\text{OD}}/f_{\text{img}})}{\pi}} = \sqrt{\frac{(D_{\text{OD}}/2)^2}{f_{\text{img}}}} \tag{2}$$

where $A_{\text{OD}} = \pi(D_{\text{OD}}/2)^2$, $D_{\text{OD}} = 1.85\,\text{mm}$.

The 1200 images from MESSIDOR database have three different formats: $1440 * 960$, $2240 * 1488$ and $2304 * 1536$ pixels. Correspondingly, we have three different estimates of the OD radius: 70, 100, and 110 pixels.

B. OD Localization Algorithm

We first find the OD candidates using template matching in the CIElab lightness image. The CIElab color space is an imaging device independent color model. Its lightness component closely matches human perception of brightness variation. In the CIElab lightness channel, the image lightness is more uniform and homogeneous in OD region than in the RGB red channel while the contrast of OD margin is high. The red channel of a color retinal image more tends to be saturated.

1) Background Normalization: To reduce the false detection of OD candidates due to nonuniform illumination, we applied an image illumination correction to the CIElab lightness image using image division. The oversmoothed background image was generated by average filtering using a square window three times the size of the estimated OD radius. The size of the filter chosen is larger than the OD in order to capture the slow-varying background. We expanded the original image border by half of the filter window size. Each pixel's intensity for the out-of-FOV dark region is replaced by averaging gray levels of pixels in the FOV. The purpose of the expansion is to remove the artifacts at the image border in the processed image due to the large size of the filter and the black background.

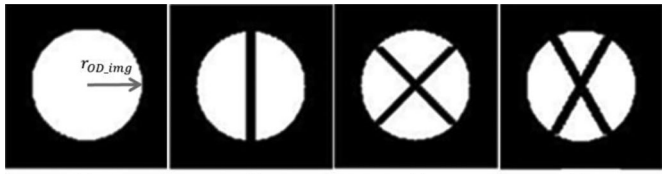

Fig. 3. Binary templates, (a) template used in the OD localization method. (b), (c), and (d) Template variations described in Section IV.

An image $f(x, y)$ can be viewed as a product of an illumination component $i(x, y)$ and a reflectance component $r(x, y)$, which depends on the imaging surface

$$f(x, y) = i(x, y)r(x, y). \tag{3}$$

A slow-varying background image can be denoted as

$$f_b(x, y) = i_b(x, y)r_b(x, y). \tag{4}$$

The new image can be expressed as

$$f(x, y)/f_b(x, y) = (i(x, y)r(x, y))/(i_b(x, y)r_b(x, y)). \tag{5}$$

We assume the reflectance of the slow-varying background image is uniform over its surface, $r_b(x, y) = k$, and the illumination of the both images is the same. Then

$$f(x, y)/f_b(x, y) = r(x, y)/k. \tag{6}$$

The resulting image is an illumination normalized image.

2) Template Matching: To locate the OD candidates a binary template where the disk, given in white, is assigned a value 1 and the black background is assigned a value 0. The radius of the white circle in the template is the estimated OD radius $r_{\mathrm{OD\_img}}$. The template width/height is set to be $3 \times r_{\mathrm{OD\_img}}$ [see Fig. 3(a)]

Since the purpose of template matching is only to provide the OD candidate locations, we accelerate the algorithm by searching on a grid (not by pixels), where each grid point is one-fourth the distance of the OD radius. The performance of this binary template is comparable to the intensity template [11], which needs to be obtained on multiple retinal images. We designed and experimented with several variations of this binary template (see Fig. 3) and found that there is no significant advantage using a specific one (see Section IV).

The Pearson correlation coefficient is used to measure the degree to which the CIElab lightness subimage and the template agree in general

$$c_{ij} = \frac{\sum_{x,y}(f(x, y) - f_m)(t(x - i, y - j) - t_m)}{\sqrt{(\sum_{x,y}(f(x, y) - f_m)^2)(\sum_{x,y}(t(x - i, y - j) - t_m)^2)}} \tag{7}$$

where t_m and f_m are the mean intensity values of the template and the subimage covered by the template, respectively. The value of c_{ij} is between -1 to $+1$.

The template matching responses were sorted in ranked order. The locations with the values in the top 0.5% of the template matching responses were selected as OD candidates.

3) Directional Matched Filtering: Some regions, such as those composed of exudates (see Fig. 4, first row), PPA (see Fig. 4, second row), and myelinated nerve fibers (see Fig. 4, third row), may also give high correlations in the template matching algorithm. We are able to remove false positives and locate the OD center by using one of the most prominent characteristics of the OD, the main vessel arcades originating from the OD center.

The intensity profile of a blood vessel cross section can be modeled by using a Gaussian kernel. A 2-D matched filter kernel is used to convolve with the green channel image in order to detect the main vessels on the OD [30]. The matched filter kernel, which matches the intensity profile of a number of vessel cross sections along the vessel length, is expressed as

$$G(x, y) = -a\, e^{-x^2/2\sigma^2}, \text{for } |y| \le \frac{L}{2} \tag{8}$$

where L is the length of the segment for which the vessel is assumed to have a fixed orientation. In (8), the direction of the vessel is assumed to be aligned along the *y*-axis to approximate the direction of the main vessels that cross the OD region. The kernel size depends on the maximum central vessel width inside the OD, which is approximately 15% of the OD diameter [31]. To increase the OD detection success rate, a rectangular region is used with each OD candidate for vertical matched filtering. The size of the rectangle region is set to $2r_{\mathrm{OD\_img}} \times 6r_{\mathrm{OD\_img}}$ The OD candidate with the maximum contrast (maximum standard deviation) in the region after matched filtering is determined to be the OD location (see Fig. 4).

C. OD Segmentation Algorithm

In some retinal images, the OD boundary may appear blurry and faint due to light scatter caused by a cataract or operator errors in the image acquisition. To address this problem, we apply a fast, hybrid level set segmentation model [32], which combines the region information and local edge vector to drive the deformable contour converging to the true OD boundary. For a more robust performance, prior to segmentation, a series of gray-scale morphological operations are applied for blood vessel and bright region removal in the ROI. These techniques are described next.

1) Image Preprocessing: There are several issues that need to be addressed prior to OD segmentation. In what follows, we provide methods for detecting red channel saturation and removing artifacts/distractors prior to segmentation.

a) Saturation detection in the red channel: In the red channel, the OD often appears with the most contrast against the background, while vessels appear less prominently. Thus, the OD segmentation algorithm is performed in red channel. Unfortunately, in some images, the red channel is saturated around the OD. This phenomenon can lead to significant degradation in performance of the OD boundary segmentation algorithm. To avoid this issue, we first detect saturation in the red channel based on the statistics of the red channel ROI. The OD segmentation ROI is a cropped subimage with the size of $6r_{\mathrm{OD\_img}} \times 6r_{\mathrm{OD\_img}}$ centered at the detected OD location. The ROI area is approximately 10 times larger than the area of the OD. This means that the 90th percentile value approaches the maximum

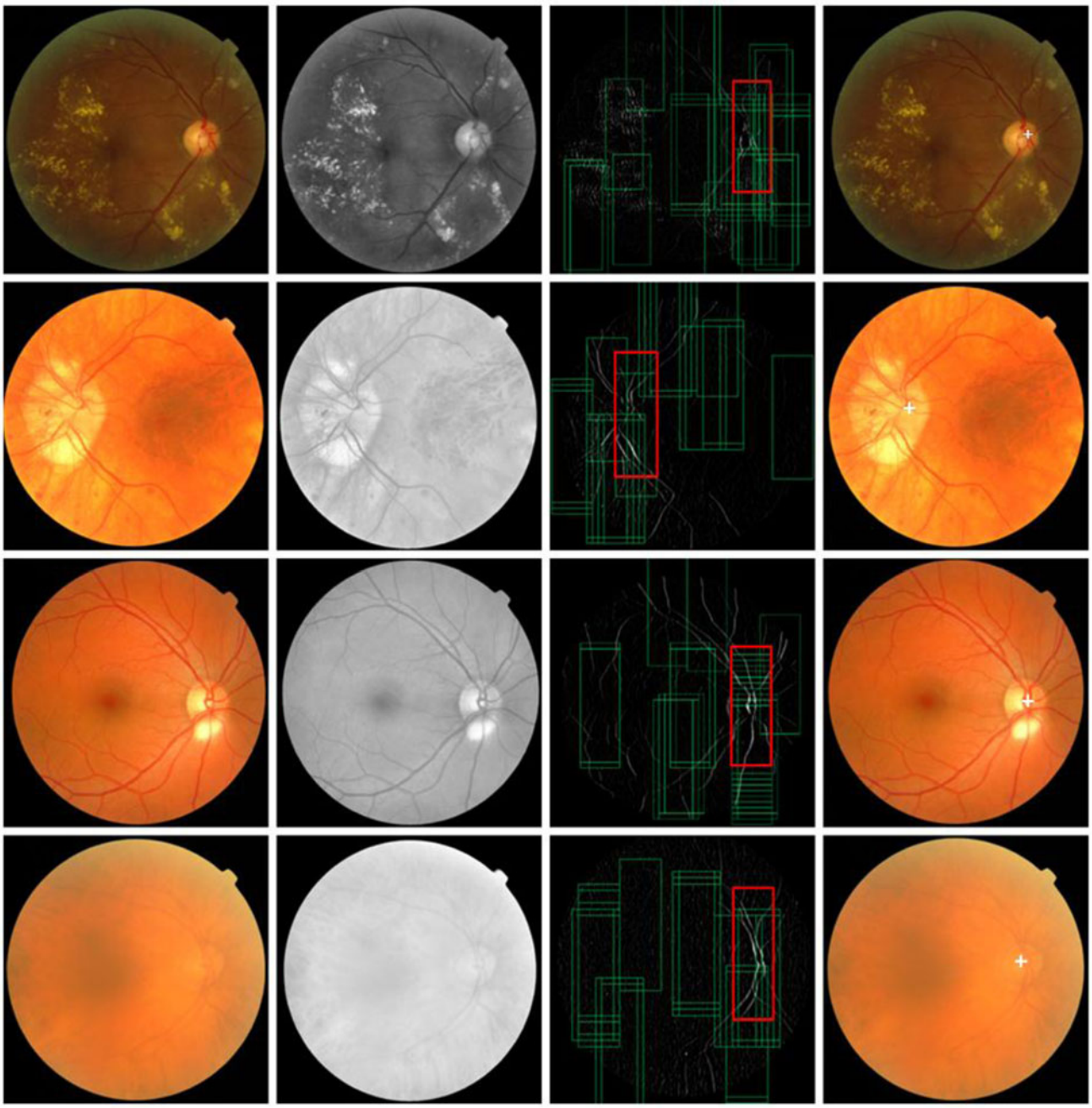

Fig. 4. OD localization examples. *First column*: Input retinal images. *Second column*: Background normalized CIElab lightness images. *Third column*: OD candidates (green) and detected OD location (red) on matched filtering response images. *Fourth column*: Results of OD localization.

intensity value in the ROI. If the red channel is saturated, there will be a large number of bright pixels in the ROI. This leads to the following red channel saturation detection rule. If half of the pixels in the ROI (50th percentile value) are brighter than the 80% of the maximum intensity value in the ROI, the red channel is assumed to be saturated. If this is the case, then the OD segmentation is performed in the CIElab lightness image.

b) Blood vessel removal: Interference of blood vessels is one of the main difficulties in accurate OD boundary segmentation. ASF is used to perform morphological close-open filtering with a series of structural elements of increasing size, which allows us to remove vessels while retaining the shape of the papillary region. We start with a symmetrical disk structural element of a radius, which is larger than the widest main vessel width in the OD region. To get a more homogeneous OD region, we use successively larger structural elements (by 10 pixels) and compute the final image using

$$g(x,y)=\gamma_{\mathrm{opn}}^{(B_n)}\{\varphi_{\mathrm{clo}}^{(B_n)}[\ldots\gamma_{\mathrm{opn}}^{(B_1)}(\varphi_{\mathrm{clo}}^{(B_1)})f(x,y)))]\}n=3 \quad (9)$$

where $\varphi_{\mathrm{clo}}^{(B_i)}=f(x,y)\odot(B_i)$ is a closing with structural element B_i, and $\gamma_{\mathrm{opn}}^{(B\_i)}=f(x,y)\odot(B_i)$ is an opening with

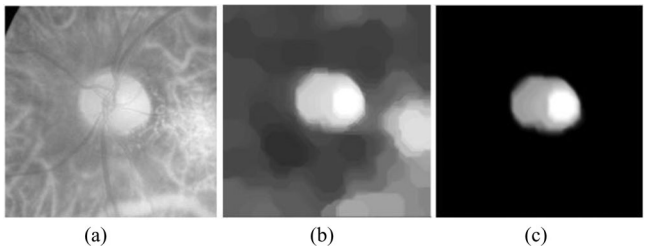

Fig. 5. Choroidal vessel removal before OD segmentation. (a) Choroidal vessels presented in the red channel. (b) Result after ASF to remove vessel*. (c) Removal of bright regions other than the OD*. *Contrast stretching was applied to the images for illustration purpose.

structural element B_i. Given the significantly larger size of the OD, the disk boundary is preserved through the use of ASF.

c) Bright region removal: In the OD segmentation ROI, areas containing features with bright pigmentation, such as choroidal vessels, exudates, and cotton wool spots may interfere with the OD boundary segmentation. We use morphological reconstruction to suppress the bright regions that are lighter than their surroundings and are also connected to the image border. Fig. 5 shows a retinal image where the bright, dense, net-like choroidal vessels are presented in the peripapillary region. The unwanted bright regions, which are connected to the ROI border after ASF, were removed by using morphological reconstruction. The shape of the papillary region remains unchanged, except for a small region on the boundary (at the inferior nasal, i.e., lower left, corner) where the blood vessels occupied originally in the input image.

We use the original image $f(x, y)$ as the mask, and the marker image $f_{mk}(x, y)$ is defined as

$$f_{mk}(x,y) = \begin{cases} f(x,y), & \text{if pixel } (x,y) \text{is on the border of } f(x,y) \\ 0, & \text{otherwise.} \end{cases} \tag{10}$$

Morphological reconstruction is the repeated dilation of the marker image until the contour of the marker image fits under the mask image. The single reconstruction step can be defined as

$$\delta_i^{(B)}(f_{\mathrm{mk}}|f) = (f_{\mathrm{mk}} \oplus B) \cap f. \tag{11}$$

where B is a structural element defined by connectivity. If 8-connectivity is used, the structural element is a 3×3 matrix of 1 s.

The reconstruction of $f(x, y)$ from marker $f_{\mathrm{mk}}(x, y)$ is defined as

$$\hat{f}(x,y) = R_f(f_{\mathrm{mk}}) = \delta_n^{(B)} \cdots \delta_1^{(B)}(f_{\mathrm{mk}}|f). \tag{12}$$

The sequential dilation is repeated until there is no further change between iterations. $R_f(f_{\mathrm{mk}})$ includes the bright regions adjacent to the ROI border. The set difference $f - R_f(f_{\mathrm{mk}})$ contains only the regions that do not touch the border in the original image, as shown in Figs. 5(c) and 6(d). The morphological reconstruction also removes bright lesions in the ROI (e.g., cotton wool spots as shown in the right column images of Fig. 6 and exudates as shown in Fig. 12, the first row).

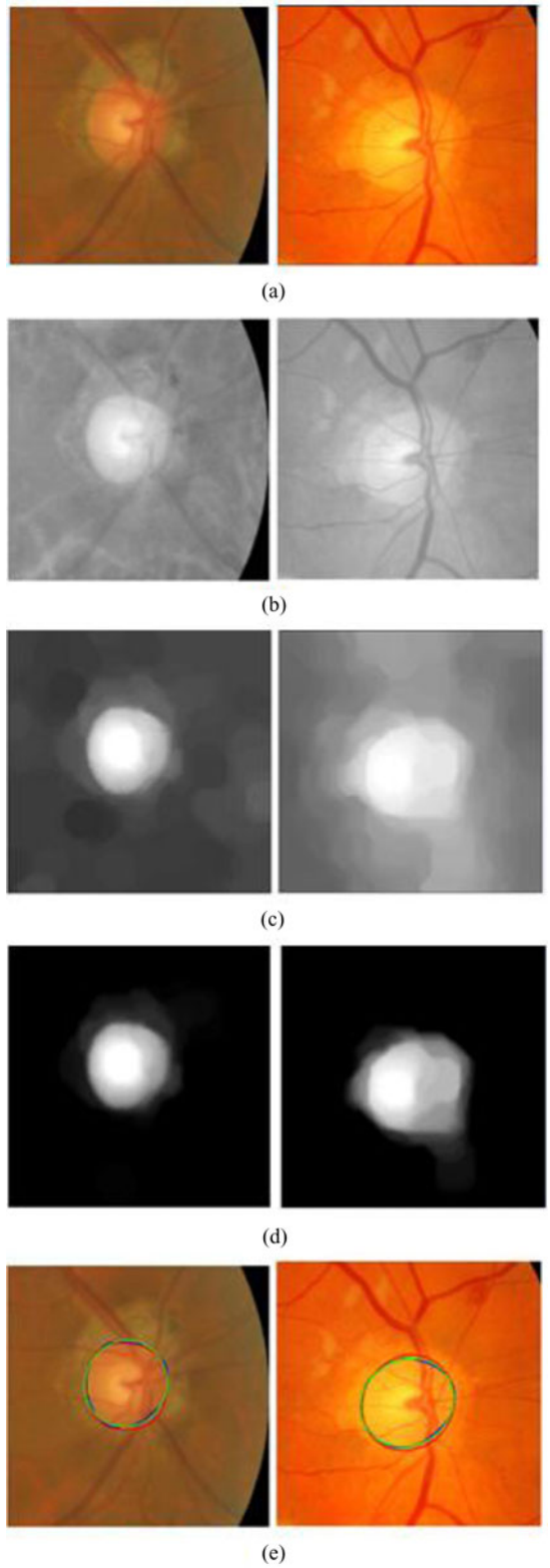

Fig. 6. OD segmentation examples. *Left column*: Segmentation on the red channel. *Right column*: Segmentation on the CIElab lighntness image. (a)I Input retinal images. (b) *Left:* Red channel image. *Right*: CIElab lightness image. (c) Images after ASF to remove vessel*. (d) Removal of bright regions other than the OD*. (e) Segmentation results (green: ellipse fitting, blue: level set segmentation, red: reference standard). *Contrast stretching was applied to the images for illustration purpose.

2) Fast, Hybrid Level Set Model: The level set methodology was first proposed by Osher and Sethian [33]. The basic idea is to embed a propagating front implicitly as the zero level set of a higher dimensional function $\varphi(x, y, t)$. It has been shown that the evolution equation for $\varphi(x, y, t)$ is obtained by

$$\frac{\partial \varphi}{\partial t} + \vec{F}|\nabla \varphi| = 0$$

with the initial condition $\varphi(x, y, t = 0) = \varphi_0(x, y)$.

The expression of the speed function $\vec{F}$ depends on the different applications. It may include many factors: local properties of the front, such as normal direction and curvature, global properties of the front, such as shape and position, and other independent external forces based on image properties that drive the propagation of the front.

A hybrid level set model was proposed in our previous study of cardiac ultrasound image video segmentation and given as [34]

$$\frac{\partial \varphi}{\partial t} = g\varepsilon k|\nabla \varphi| - (1 - s(x, y))[\beta_1((u(x, y), v(x, y)) \cdot \nabla \varphi)] + s(x, y)\beta_2 \nabla g \cdot \nabla \varphi \quad (13)$$

where the level set front is driven by the internal force curvature k and the external forces: the GVF $(u(x, y), v(x, y))$ [35] or the edge vector ∇g. Here, g is defined as an enhanced edge indicator applied to the Gaussian smoothed image given by

$$g(x, y) = \frac{1}{[1 + (|\nabla(G_\sigma(x, y) * I(x, y))|/\gamma)^2]} \quad (14)$$

where γ is a constant coefficient.

The GVF allows the curve to have relatively free initialization and quick deformations at the homogenous region at the beginning of deformation. Later, when the curve approaches the object boundaries, the edge vector field dominated the deformation to reduce edge leaking. $s(x, y)$ is a step function defined as

$$s(x, y) = \begin{cases} 0, & \text{Ave}_{\varphi(x,y,t)=0}(e(x, y)) < T_{\text{res}} \\ 1, & \text{Ave}_{\varphi(x,y,t)=0}(e(x, y)) \geq T_{\text{res}} \end{cases} \quad (15)$$

where $e(x, y)$ is an image edge map function defined by

$$e(x, y) = \left(\frac{|\nabla(G_\sigma(x, y) * I(x, y))|}{\rho} \right)^2. \quad (16)$$

The value of $s(x, y)$ is determined by the average of the edge map over the current zero level-set at each iteration.

Since GVF is computed as a spatial diffusion of the gradient of the edge map of an image, it is computationally time consuming and the GVF model is subjected to leakage problem at the poor edges where the edge map cannot be well defined. In order to meet the requirement of quick and robust OD segmentation in retinal images, we used region information instead of GVF in the hybrid level set model, as suggested by Zhang [32]. Region-based model was originally proposed by Chan and Vese [25], which is extremely effective to detect objects with fuzzy, smooth boundaries, which could not be well defined by gradient.

The new hybrid level set model is not only as robust to its curve initialization as the GVF hybrid model but also adds a more powerful stopping function at weak edges by using region intensity information besides the edge force. The curve evolution partial differential equation (PDE) is given by

$$\frac{\partial \varphi}{\partial t} = g\varepsilon k|\nabla \varphi| + \beta_1(1 - \lambda)|\nabla \varphi| + \beta_2 \nabla g \cdot \nabla \varphi. \quad (17)$$

The first term on the right-hand side in (17) is a front evolution driven by the internal curvature k. The second term represents a deformation driven by the region information I. For a bright target object, it indicates an expansion movement for the parts of the curve inside the object if $I > \lambda$ and a contraction movement for the parts of the curve outside the object if $I < \lambda$. The predefined threshold λ is the lower bound of the bright OD region intensity. The third term is the edge vector that helps to stop the evolving curve at the OD boundary. $\varepsilon, \beta_1, \beta_2$ are the parameters to control the balance of the forces.

Zhang *et al*. [32] used a fast and unconditionally stable finite difference method to solve the aforementioned PDE. It is called the additive operator splitting (AOS) approach [36].

To use the AOS approach, we simplify the PDE (17) into

$$\frac{\partial \varphi}{\partial t} = \alpha(1 - \lambda) + \beta \operatorname{div}(g\nabla \varphi) \quad (18)$$

where φ is a signed distance function (SDF) defined in the level set model, i.e., $|\nabla \varphi| = 1$, using $\alpha = \beta_1$, $\beta = \varepsilon = \beta_2$, and $k = \operatorname{div}(\nabla \varphi/|\nabla \varphi|)$, The PDE (18) is then solved efficiently by using the AOS approach.

The threshold λ should be set at the lower bound of the OD region intensity. We set the value of λ based on the contrast estimation in the ROI using

$$\lambda = \mu + c\sigma \quad (19)$$

where μ and σ are the mean and standard deviation of the ROI intensity after preprocessing, and c is a coefficient set as described next. Since the OD only occupies less than one-tenth of ROI, the mean intensity of the ROI is dominated by the intensity of the background. We consider $1 < c < 3$ to make the threshold λ higher in order to distinguish the OD from the background.

Fig. 6 shows the segmentation results of two sample images using the red channel and the CIElab lightness image, depending on the saturation condition. The OD is surrounded by PPA in the left image and cotton wool spots are presented in the right image in (a). Good segmentation results were achieved by using the proposed morphological preprocessing and the fast, hybrid level set model.

3) Segmentation Parameter Optimization: It is important to optimize the parameters, since we observed that the model performance is sensitive to the parameter setting. Zhang *et al*. [32] developed this model on head-and-neck CT images without specifying how to choose appropriate values for the threshold and parameters. Other researchers [21], [22], [24] who have used active contour models set the parameters heuristically.

The hybrid model requires presetting a single region threshold λ. As stated previously, there is great variation in OD appearance, and the contrast between the OD and the background may vary substantially. Even if the threshold λ is set based on the image contrast estimation, we still need to predefine the coefficient

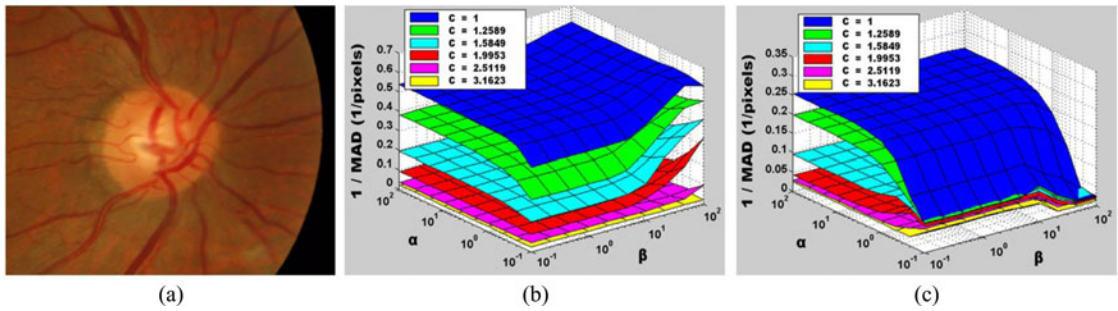

Fig. 7. Parameter optimization for the high contrast OD segmentation. (a) ROI image. (b) Red channel parameter surface as a function of α and β for six different values of c. $c = 1.0$ with minimum MAD of 1.6 pixels ($\alpha = 0.21$, $\beta = 46.41$). (c) CIElab lightness parameter surface. $c = 1.0$ with minimum MAD of 3.9 pixels ($\alpha = 10$, $\beta = 46.41$).

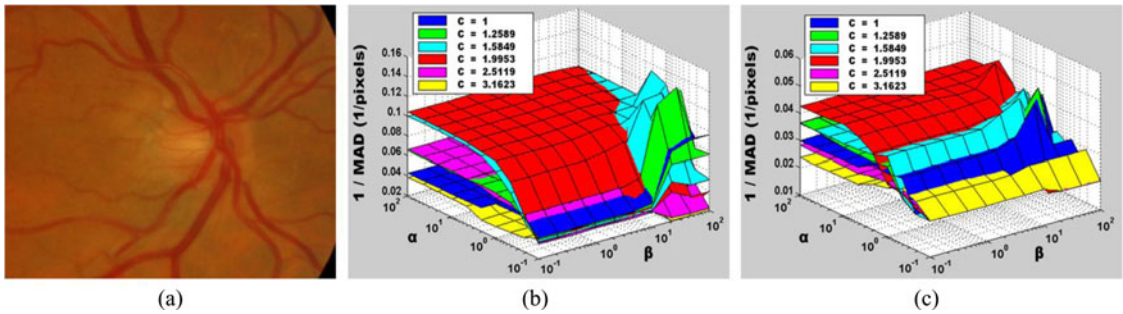

Fig. 8. Parameter optimization for the low contrast OD segmentation. (a) ROI image. (b) Red channel parameter surface as a function of α and β for six different values of c. $c = 1.25$ with minimum MAD of 7.0 pixels. ($\alpha = 0.21$, $\beta = 46.41$). (c) CIElab lightness parameter surface. $c = 1.99$ with minimum MAD of 17.8 pixels ($\alpha = 10$, $\beta = 46.41$).

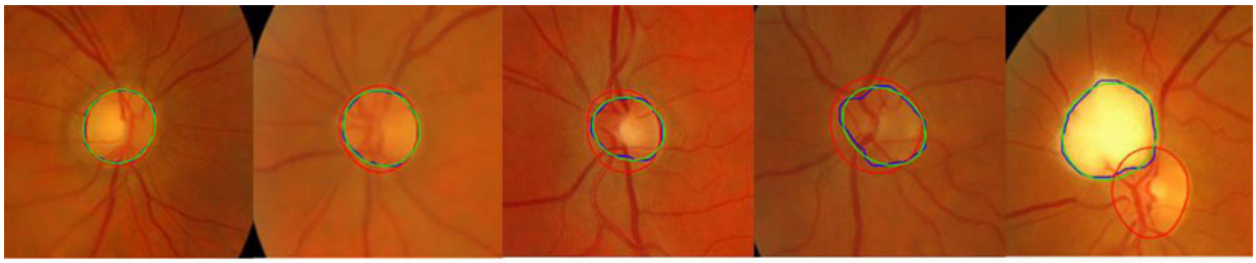

Fig. 9. Segmentation examples ($r_{\mathrm{OD\_img}} = 100$ pixels). (a) Excellent, MAD = 3.0 pixels. (b) Good, MAD = 8.2 pixels. (c) Moderate, MAD = 14.7 pixels. (d) Fair, MAD = 21.6 pixels. (e) Poor, MAD = 93.4 pixels (green: ellipse fitting, blue: level set segmentation, red: reference standard).

c in order to obtain an accurate segmentation. The parameters α and β can also affect the performance of the model. For example, if the value of α is too small, the evolution front may not be able to converge on the true boundary quickly. For very high values of β, the evolving curve may pass through the true boundary, a result of leakage at the weak, blurry edges. Furthermore, the values of the parameters may affect the model performance in an interrelated and complex way. Therefore, it is necessary to consider the possible values in a large range for the parameters in the optimization.

We used a logarithmic sampling, which generates logarithmically spaced values and covers a wide range of possible values of the parameters. Logarithmic sampling does capture the variation in the data while requiring fewer samples than linear space sampling. The coefficient c is set as $c = [1.00, 1.25, 1.58, 1.99, 2.51, 3.16]$ to cover the sampling values between 1 and 3. Logarithmic scale sampling is also considered for α and β. A total of ten different values per parameter are set as [0.10, 0.21, 0.46, 1.00, 2.15, 4.64, 10.00, 21.54, 46.41, 100.00] to represent the changes in a wide range of values for the parameters.

To evaluate segmentation performance for each parameter combination, two representative test images were selected, one with high OD contrast and another with low OD contrast and strong vessel interference. Parameter optimization was performed both on the red channel and CIElab lightness for each image. The mean absolute distance (MAD) between the reference standard and the automatically segmented boundaries is used to determine the optimal parameters. Figs. 7 and 8 show the images and the optimization plots for the red channel and CIElab lightness images. For better visualization, we plot the parameter surfaces in term of the inverse of MAD (i.e., 1/MAD).

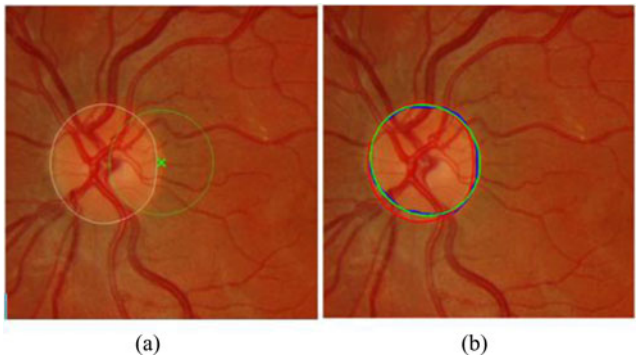

Fig. 10. Robustness to curve initialization. (a) ROI image ($r_{\mathrm{OD\_img}} = 100$ pixels) with segmentation initialization in green, reference standard in white. (b) Segmentation result, MAD = 8.3 pixels (green: ellipse fitting, blue: level set segmentation, red: reference standard).

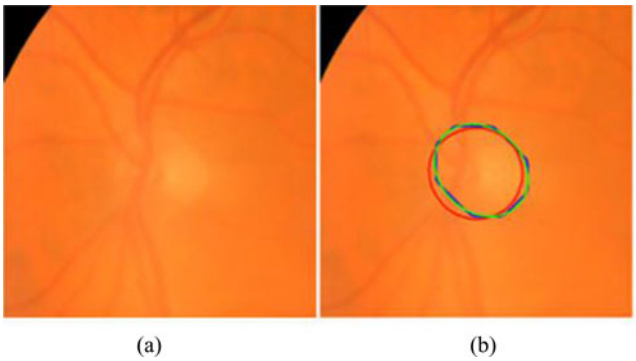

Fig. 11. Blurred OD boundary segmentation. (a) ROI image ($r_{\mathrm{OD\_img}} = 70$ pixels). (b) Segmentation result, MAD = 6.9 pixels (green: ellipse fitting, blue: level set segmentation, red: reference standard).

This suggests that the best parameters are the ones that make 1/MAD reach the highest value.

For the high contrast OD image, the minimum MAD is achieved for $\alpha = 0.21, \beta = 46.41, c = 1.0$ in the red channel and $\alpha = 10, \beta = 46.41, c = 1.0$ in CIELab lightness (see Fig. 7). The large difference in α values suggests that the curve needs to be driven by a stronger region force in the lightness image than in the red channel image, since the lightness images have lower contrast than the red channel image. We reach a similar conclusion for the low OD contrast images. The minimum MAD is achieved for $\alpha = 0.21, \beta = 46.41, c = 1.25$ in the red channel and $\alpha = 10, \beta = 46.41, c = 1.99$ in the CIELab lightness (see Fig. 8). By comparing the coefficient c for both the red channel and the CIElab lightness images, we note that the coefficient c is larger in the CIElab lightness image segmentation than in the red channel image. Based on the aforementioned parameter optimization analysis, we obtained the optimum parameters listed in Table I. For achieving reasonable performance over a wide range of images, we adjusted the value of coefficient c to be the average of the optimal coefficient values estimated for both the high OD contrast and low OD contrast images.

It is interesting to note that the optimization level is relatively flat within a certain region of the $\alpha - \beta$plane in the four parameter surface plots shown in Figs. 7 and 8. In particular, the heuristically derived parameters given by $\alpha = 10, \beta = 1$ (used in our earlier investigations [37]) are within the flat region, which gives suboptimal performance.

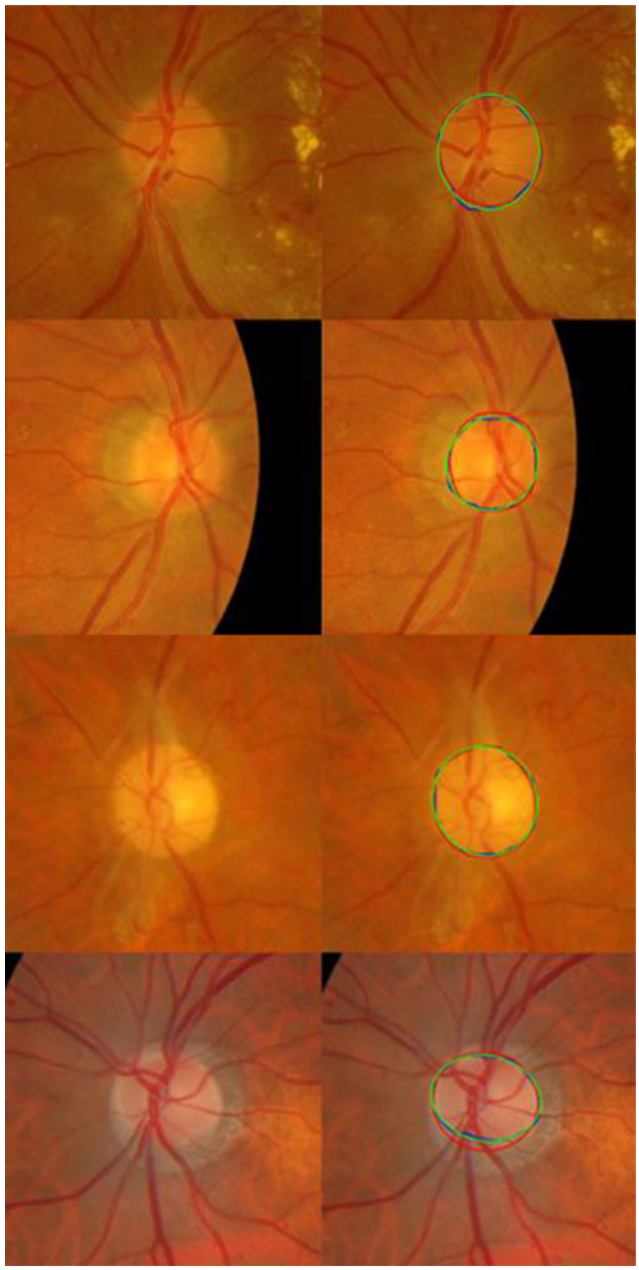

Fig. 12. Segmentation examples of challenging cases (green: ellipse fitting, blue: level set segmentation, red: reference standard).

TABLE I
OPTIMIZED PARAMETERS FOR HYBRID LEVEL SET MODEL

	α	β	c
Red Channel	0.2	50	1.1
CIElab Lightness	10	50	1.5

4) Least-Square Ellipse Fitting: The curvature is used to define an internal force to make the evolving contour smooth during the hybrid level set model deformation. The final curve may still appear irregular due to the influence of strong blood

TABLE II
OD DETECTION FOR THE NUMBER OF IMAGES IN EACH RETINAL PATHOLOGY GRADE AND NUMBER OF FAILURES GIVEN IN PARENTHESIS

	ME Risk 2	ME Risk 1	ME Risk 0
DR Grade 3	111 (4)	42 (0)	107 (0)
DR Grade 2	37 (0)	28 (0)	182 (0)
DR Grade 1	6 (0)	5 (0)	142 (1)
DR Grade 0	-	-	540 (6)
Total		1200 (11)	

vessels. To provide for a smooth contour, we fit the segmented OD boundary with an ellipse using the least-squares optimization. This step generates smooth OD borders that can be used for cup-to-disk ratio computation in glaucoma analysis for future study.

III. RESULTS

A. Datasets

The MESSIDOR database was created to facilitate studies on computer-aided diagnoses of DR (http://messidor.crihan.fr). The database contains 1200 color fundus images of the posterior pole acquired by three ophthalmologic departments using a color 3CCD camera on a Topcon TRC NW6 nonmydriatic retinograph with a 45° FOV. Eight hundred images were acquired with pupil dilation (one drop of Tropicamide at 10%) and 400 without dilation. The images were captured at three different image sizes: 1440 × 960, 2240 × 1488, and 2304 × 1536 pixels.

Two diagnoses were provided for each image: grade of DR and risk of macular edema. There are four grades for retinopathy. Grade 0 means no retinopathy, grades 1 and 2 correspond to patients with nonproliferative retinopathy (NPDR), and grade 3 corresponds to patients with severe NPDR or proliferative DR. There are three grades for risk of macular edema. Grade 0 corresponds to normal images (no visible hard exudates), grade 1 to images with exudates located more than 1 disk-diameter away from the fovea, and grade 2 to images with exudates located within 1 disk-diameter of the fovea (highest risk of macular edema).

The OD boundary reference standard for the 1200 images is publicly available and kindly provided by the University of Huelva, Spain (http://www.uhu.es/retinopathy) [26]. They divided the database into four subsets and each subset was graded by a different single observer using computer software.

B. OD Localization

The results of OD detection in this study were obtained based on the original input image resolution. If the detected OD center is within the circumference of the OD in the reference standard, then it is considered to be a successful detection. The algorithm correctly located the OD in 1189 out of the 1200 images, a success rate of 99.1%. Table II presents the results according to the level of retinopathy and the risk of macular edema graded by the MESSIDOR specialists.

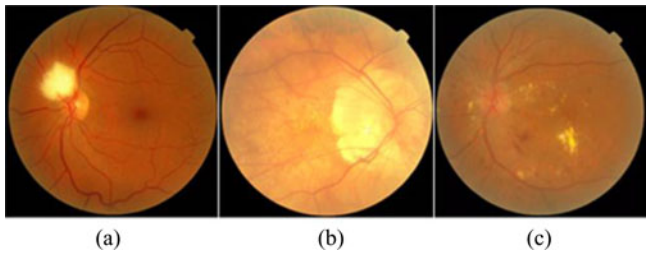

Fig. 13. OD detection failure examples. (a) Large myelinated nerve fiber. (b) Extra-large and bright PPA overshadows the OD. (c) Retinal image with grade 3 DR and grade 2 risk of macular edema.

There are 11 images in which the algorithm did not accurately locate the ODs. This was due to three factors: 1) advanced stage of retinopathy and presence of exudate clusters (four images), 2) large myelinated nerve fibers adjacent to the OD, which were much brighter [two images, an example is shown in Fig. 13(a)], 3) severe peripapillary atrophies, whose size and brightness completely overshadowed the OD [five images, an example is shown in Fig. 13(b)]. In other cases, the OD was selected in the candidates regardless of the presence of myelinated nerve fibers and peripapillary atrophies in the images, and the proposed OD detection algorithm worked well (see Fig. 4, the second and third row).

C. OD Segmentation

The initial contour of the deformable model is automatically set as a circle with the center at the detected OD location and the radius as the estimated OD radius $r_{\mathrm{OD\_img}}$. The performance of the OD segmentation algorithm is quantitatively evaluated using the MAD. MAD measures the average difference between two contours, and is obtained by averaging the distance to the closest point (DCP) of all the points on the two curves. If two curves Γ_1 and Γ_2 can be represented as finite sets of points $\Gamma_1 = (n_1, n_2, \ldots, n_p)$ and $\Gamma_2 = (m_1, m_2, \ldots, m_q)$, The DCP for n_i on the curve Γ_1 to the curve Γ_2 is defined as

$$d(n_i, \Gamma_2) = \min_j ||m_j - n_i||. \tag{20}$$

The MAD between the two curves is defined as follows:

$$M(\Gamma_1, \Gamma_2) = \frac{1}{2}\left[\frac{1}{p}\sum_{i=1}^{p} d(n_i, \Gamma_2) + \frac{1}{q}\sum_{j=1}^{q} d(m_j, \Gamma_1)\right]. \tag{21}$$

To evaluate the OD segmentation algorithm independently of OD detection, OD centers were manually located for the 11 images in which the OD localization fails. For the optimized results, we use the optimal parameters obtained by following the optimization method that we described in Section II. Only the coefficient c was slightly tuned for the images acquired from three different ophthalmologic departments. We note that evaluating the algorithm performance in terms of MAD in pixels alone is not informative unless the size (and, hence, resolution) of the image being analyzed is given. Instead of using MAD alone, we use the ratio of MAD and the estimated OD radius for our algorithm evaluation. Table III shows the evaluation

TABLE III
OD SEGMENTATION EVALUATION USING THE RATIO OF MAD OVER THE ESTIMATED OD RADIUS (1200 IMAGES)

Categories	MAD/r_{OD_img}	Percentage
Excellent	$\leq (1/20)$	33%
Good	$\leq (1/10)$	68%
Moderate	$\leq (1/5)$	89%
Fair	$\leq (1/3)$	97%

TABLE IV
CORRELATION COEFFICIENTS BETWEEN DIFFERENT BINARY TEMPLATES

	R_{aa}	R_{ab}	R_{ac}	R_{ad}
R_{aa}	1.0	0.91	0.88	0.85
R_{ba}		1.0	0.80	0.79
R_{ca}			1.0	0.78
R_{da}				1.0

results on 1200 images from MESSIDOR database, without excluding any images for poor quality. Qualitatively, we use five categories of segmentation quality (Excellent, Good, Moderate, Fair and Poor), as defined by other investigators in [22] and [24], depending on the ratio of MAD and the OD radius $r_{\mathrm{OD\_img}}$. Fig. 9 shows examples in each category. The ratio of MAD and OD radius corresponds reasonably well to the qualitative assessment of segmentation quality. Table III shows that MAD is not larger than one-tenth of the OD radius for 68% of 1200 images, corresponding to the excellent to good segmentation quality. MAD is less than or equal to one-third of the OD radius for 97% of the images in the database, corresponding to the excellent to fair quality range. The average MAD of 1200 images was 10.1% of the OD radius, regardless of the different image sizes in the database.

An example of the robustness of the fast, hybrid level set model to the curve initialization is shown in Fig. 10. The automatically initialized contour intersected the OD boundary, due to the offset between the located OD and true OD center. The fast, hybrid level set model has the ability to drive the contour to enclose the regions with intensities greater than certain threshold value even though the initialization is not "perfect." Our segmentation model is robust in regard to the variations in segmentation initialization from the prerequisite detected OD locations, compared to previous active contour models reported in [21] and [22].

The algorithm also performs well on the images with a blurred OD margin due to severe cataracts (see Fig. 11). Thanks to the region intensity information in the fast, hybrid level set model, the evolving contour converges to the true OD boundary even in the indistinct, blurred OD images.

Fig. 12 shows the segmentation results for a few challenging cases. The first row presents an example of fuzzy boundary at the bottom of disk with exudates in the ROI. The second row shows an example of optic nerve hypoplasia, an underdevelopment of tissue, with a crescent region adjacent to the disk. Vitreous strands cause traction on optic nerve head vessel in the third row of images. The last row presents an example of PPA.

The segmentation results shown in Fig. 12 indicate that with carefully designed preprocessing morphological techniques, the fast, hybrid level set algorithm, which combines the region information and local image gradient, performs well on these difficult cases.

IV. DISCUSSION

A. Template Design in OD Detection

Several researchers have applied different templates to detect the OD location [11], [12], [22]. We investigated the effect of different templates in OD detection. There is no observed significant performance improvement using a particular binary template. This conclusion was verified by the computation of correlation coefficient between the different templates. We designed four binary templates shown in Fig. 3. The black bands inside the white disk approximate the main vessels inside the OD in order to improve template matching performance. The correlation coefficients R_{cc} between the different templates are shown in Table IV. If we compare the first template (a) with the other three templates [(b)–(d)], the lowest R_{cc} is 0.85, which indicates there is no significant difference between these templates. This conclusion is also verified by our experiment results. We used the second template (b) in our OD detection. This template is the same as the one used by Lowell *et al*. [22], which is composed of the Laplacian of Gaussian with a vertical channel in the middle to correspond to the main vessel band in the OD. Since the vertical black band in the template may have a false high correlation to the OD margin at the temporal side, instead of the main vessels inside the OD, when uneven brightness was present in the OD region, the template (b) did not exhibit a better performance than the template (a) in OD detection.

The advantage of our OD detection methodology is that we exploit the vessel characteristics within the OD after template matching. This technique increases the robustness and accuracy of OD detection.

It should be noted that our OD detection algorithm fails in well-understood circumstances. First, the algorithm fails on retinal images in which the OD is darker than the surrounding pixels, such as when a large, very bright myelinated nerve fibers or severe PPA is adjacent to the OD [see Fig. 13(a) and (b)]. Second, advanced DR and bright exudates clusters affect the accuracy and success of our algorithm. An example image with grade 3 DR and grade 2 risk of macular edema is shown in Fig. 13(c). Third, the algorithm cannot deal with retinal images where the OD does not appear as a circular brightness structure and main vessels are not presented in OD region (for example, images with the advanced stage of papilledema).

The proposed OD localization methodology provides sufficient accuracy and speed for high workloads in automatic eye screening. The average running time was 4.7 s per image (1440×960) on an Intel Xeon CPU W3520, 2.67 GHz, 6 GB

RAM computer. The algorithm was implemented in MATLAB R2010b (MathWorks).

B. OD Segmentation Comparison

To compare the results obtained by Aquino *et al.* [26] on the same database (MESSIDOR), we also compute the overlapping ratio between the segmented OD areas A_s and the OD regions A_g marked in reference standard, defined as

$$R = \frac{A_s \cap A_g}{A_s \cap A_g}. \tag{22}$$

The average area overlapping ratio between the automatic segmented OD boundary and the reference standard for the 1200 images is 84.4%, which is slightly lower than the ratio of 86% obtained by using the circle Hough transform method proposed by Aquino *et al.* [26]. The deformable model-based approach is sensitive to nonhomogeneousness, and the irregular boundary of the object. Therefore, our deformable model generates more accurate OD segmentations than the circle Hough transform when the OD boundaries have good to fair intensity contrast (see Fig. 14, the first and second row images). It also performs well on images with blurred OD (see Fig. 11). However, if blurry, low contrast ODs are accompanied with very dark vessel branches on the OD, the contrast and brightness of the OD border were decreased largely after morphological vessel removal, due to the darkness of the vessels. The segmented OD boundary may deviate from the true OD margin due to the sensitivity to low-contrast object of the deformable model (see Fig. 14, the third and fourth row images). In contrast to the deformable models, the circle Hough transform method [26] performs better in such cases, since only portions of the OD border were needed to obtain a fitting circle with a certain radius, which corresponds to the highest number of votes in the parameter space. Although the circle Hough transform method turns out to be a more reliable solution by matching circles on images with low contrast ODs and dark vessels, it is not able to provide sufficient accurate quantitative measurements of the OD boundary for OD pathological change analysis overall, e.g., glaucoma. The level set model offers a more accurate approach for glaucoma analysis, which is normally preformed on OD-centered images with better OD contrast conditions. Both the hybrid level set model and the circle Hough transform approach are sensitive to bright myelinated nerve fibers adjacent to the OD (see Fig. 14, the fifth row images). To the best of our knowledge, these cases could affect most disk boundary segmentation algorithms.

In order to compare the computer-to-observer agreement and the interobserver agreement, 100 images were randomly selected from the database. The OD boundaries of these images were manually marked by an ophthalmologist independently. The average MAD, Hausdroff distance, and the overlapping ratio as well as standard deviations obtained by comparing the segmentations between the reference standard (grader 1), the grading provided by the ophthalmologist (grader 2), and the automated method are listed in Table V. The Haudorff distance measures the maximum difference between the corresponding points on the two curves. The values of the three segmentation

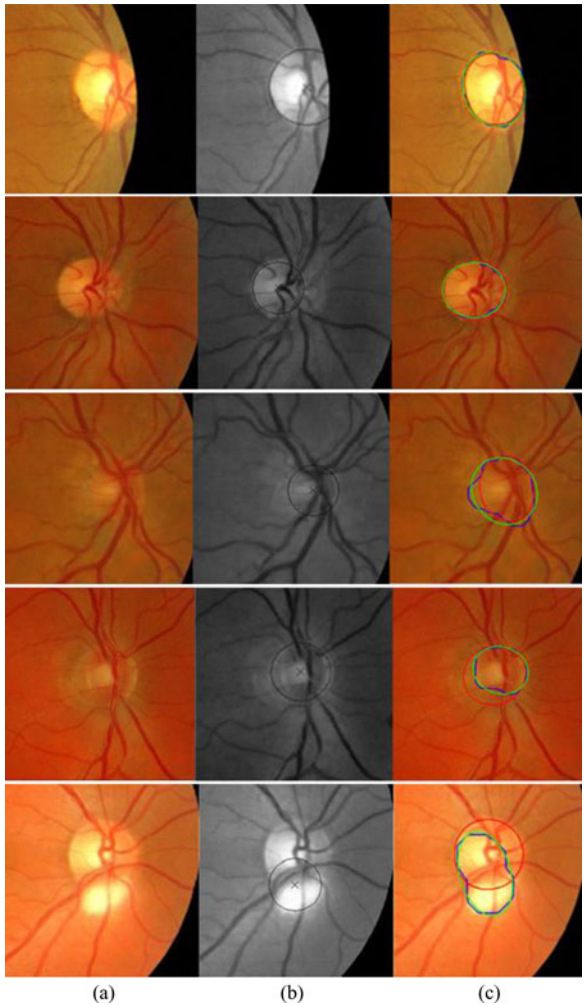

Fig. 14. OD segmentation comparison. (a) Retinal images. (b) Segmentation by Aquino *et al.* [26] (http://www.uhu.es/retinopathy/disco_optico2.php). (c) Segmentation by the proposed method (green: ellipse fitting, blue: level set segmentation, red: reference standard). In the fourth rows, the OD boundary marked in reference standard (red) is inaccurate due to the tilted OD.

TABLE V
COMPARISON OF OD BOUNDARY SEGMENTATIONS

	MAD	Hausdroff	Overlapping Ratio
Grader 1 vs. Grader 2	4.87 (3.85*)	13.41 (9.46)	*88.9% (6.9%)*
Automated method vs. Grader1	7.73 (6.16)	18.54 (14.22)	86.5% (9.5%)
Automated method vs. Grader 2	7.79 (6.94)	19.45 (15.68)	85.7% (10.9%)

* standard deviation

metrics in Table V indicate that the computer-generated boundaries differ from the manually outlined boundaries slightly larger than the manually outlined boundaries differ from one another.

We used the William agreement index to present how each grader can be compared with the set composed of the remaining two graders by adding the automated method's segmentation as

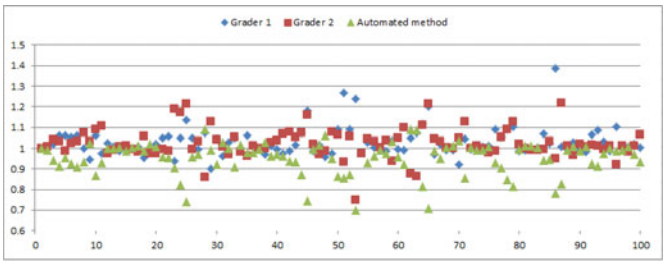

Fig. 15. Williams agreement index (using overlapping ratio as similarity measure).

TABLE VI
WILLIAMS AGREEMENT INDEX WITH 95% CONFIDENCE INTERVAL FOR OD SEGMENTATIONS

	WI	95% CI
Grader 1	1.05	(1.02, 1.08)
Grader 2	1.02	(1.01, 1.04)
Automated method	0.95	(0.93, 0.98)

a third observer's grading [38], [39]. William index is defined as

$$\mathrm{WI}_i = \frac{(n-2)\sum_{j\neq i}^{n} R_{ij}}{2\sum_{j\neq i}^{n}\sum_{k\neq i}^{j-1} R_{jk}}$$

where R_{ij} is the overlapping ratio (i.e., similarity measures) for a pair of segmentations and n is the number of graders (segmentations). The William index computes the ratio between the average agreement between one grader (e.g., grader i), each of the remaining graders and the average interobserver agreement except grader i. Fig. 15 shows the William indices of three graders, if the automated approach is counted as the third grader.

The average William indices and 95% confidence intervals (CI) of the grader 1, 2, and the automated method are shown in Table VI. The CI for the index was estimated using a jackknife nonparametric sampling technique [40]. This sampling procedure was implemented by leaving out one of the images at a time and computing the Williams index using the overlapping ratio for $N-1$ images. If the upper limit of the 95% CI is greater than the value one, we can conclude that the individual grader agrees with the group at least as well as the group members agree with each other [41]. Here, the upper limit of the CI of the automated method is 0.98, the automated method agrees with the two human graders nearly as well as the two human graders agree with each other.

The average computation time for OD segmentation was 6.6 s per image (1440 $\times$ 960) with the same computer and software specified in the OD detection discussion. Considering the fact that the high accuracy of manual segmentation was obtained at a cost of long hand-segmenting time and heavy work load, the proposed automated method has the advantage of providing up to 10 times faster speed with sufficient accuracy to meet automatic analysis system requirements.

V. CONCLUSION

A new, fast, and robust OD localization and segmentation methodology for retinal image screening has been developed. The OD localization methodology adaptively changes the template size based on the OD radius estimation, using the camera FOV and the image resolution. The methodology not only exploits the appearance features of the OD, but also main vessel orientation inside the OD, to increase robustness. The OD segmentation method uses ASF and morphological reconstruction to remove vessels and bright region distractors while retaining the shape of the papillary region. The fast, hybrid level set model uses both region information and local edge vector with simple automatic initialization to achieve robust, fast, and accurate segmentation. The model parameters are optimized for the best segmentation performance.

The future automatic eye disease screening system will have to be robust, fast, and provide high accuracy rates in order to support high workloads and near-real-time operation. The methodology developed herein has been designed to satisfy these requirements. The robustness and efficiency makes this methodology suitable for assisting automatic screening for early signs of eye diseases.

ACKNOWLEDGMENT

The authors would like to thank S. Nemeth, Certified Ophthalmic Medical Technologist (COMT) and R. Crammer, Doctor of Optometry (OD), for their valuable clinical observations, and E. McGrew for her editorial assistance.

REFERENCES

[1] D. Usher, M. Dumskyj, M. Himaga, T. H. Williamson, S. Nussey, and J. Boyce, "Automated detection of diabetic retinopathy in digital retinal images: A tool for diabetic retinopathy screening," *Diabetic Med.*, vol. 21, pp. 84–90, 2004.

[2] A. D. Fleming, K. A. Goatman, S. Philip, G. J. Prescott, P. F. Sharp, and J. A. Olson, "Automated grading for diabetic retinopathy: A large-scale audit using arbitration by clinical experts," *Br. J. Ophthalmol.*, vol. 94, pp. 1606–1610, Dec. 2010.

[3] C. Agurto, V. Murray, E. Barriga, S. Murillo, M. Pattichis, H. Davis, S. Russell, M. Abramoff, and P. Soliz, "Multiscale AM-FM methods for diabetic retinopathy lesion detection," *IEEE Trans. Med. Imag.*, vol. 29, no. 2, pp. 502–512, Feb. 2010.

[4] K. A. Goatman, A. D. Fleming, S. Philip, G. J. Williams, J. A. Olson, and P. F. Sharp, "Detection of new vessels on the optic disc using retinal photographs," *IEEE Trans. Med. Imag.*, vol. 30, no. 4, pp. 972–979, Apr. 2011.

[5] G. D. Joshi, J. Sivaswamy, and S. R. Krishnadas, "Optic disk and cup segmentation from monocular color retinal images for glaucoma assessment," *IEEE Trans. Med. Imag.*, vol. 30, no. 6, pp. 1192–1205, Jun. 2011.

[6] R. J. Winder, P. J. Morrow, I. N. McRitchie, J. R. Bailie, and P. M. Hart, "Algorithms for digital image processing in diabetic retinopathy," *Comput. Med. Imag. Graph.*, vol. 33, pp. 608–622, 2009.

[7] A. Youssif, A. Z. Ghalwash, and A. Ghoneim, "Optic disc detection from normalized digital fundus images by means of a vessels' direction matched filter," *IEEE Trans. Med. Imag.*, vol. 27, no. 1, pp. 11–18, Jan. 2008.

[8] C. Sinthanayothin, J. F. Boyce, H. L. Cook, and T. H. Williamson, "Automated localisation of the optic disc, fovea, and retinal blood vessels from digital colour fundus images," *Br. J. Ophthalmol.*, vol. 83, pp. 902–910, Aug. 1999.

[9] L. Huiqi and O. Chutatape, "Automatic location of optic disk in retinal images," in *Proc. Int. Conf. Image Process.*, 2001, vol. 2, pp. 837–840.

[10] T. P. Karnowski, V. P. Govindasamy, K. W. Tobin, and E. Chaum, "Locating the optic nerve in retinal images: Comparing model-based and

bayesian decision methods," *28th IEEE Eng. Med. Biol. Soc.*, Aug. 2006, pp. 4436–4439,.
[11] A. Osareh, M. Mirmehdi, B. Thomas, and R. Markham, "Comparison of colour spaces for optic disc localisation in retinal images," in *Proc. 16th Int. Conf. Pattern Recog.*, 2002, vol. 1, pp. 743–746.
[12] M. Lalonde, M. Beaulieu, and L. Gagnon, "Fast and robust optic disc detection using pyramidal decomposition and Hausdorff-based template matching," *IEEE Trans. Med. Imag.*, vol. 20, no. 11, pp. 1193–1200, Nov. 2001.
[13] A. E. Mahfouz and A. S. Fahmy, "Fast localization of the optic disc using projection of image features," *IEEE Trans. Image Process.*, vol. 19, no. 12, pp. 3285–3289, Dec. 2010.
[14] S. J. Lu and J. H. Lim, "Automatic optic disc detection from retinal images by a line operator," *IEEE Trans. Biomed. Eng.*, vol. 58, no. 1, pp. 88–94, Jan. 2011.
[15] A. D. Fleming, K. A. Goatman, S. Philip, J. A. Olson, and P. F. Sharp, "Automatic detection of retinal anatomy to assist diabetic retinopathy screening," *Phys. Med. Biol.*, vol. 52, pp. 331–345, Jan. 2007.
[16] M. Niemeijer, M. D. Abramoff, and B. van Ginneken, "Segmentation of the optic disc, macula and vascular arch in fundus photographs," *IEEE Trans. Med. Imag.*, vol. 26, no. 1, pp. 116–127, Jan. 2007.
[17] M. Niemeijer, M. D. Abramoff, and B. van Ginneken, "Fast detection of the optic disc and fovea in color fundus photographs," *Med. Image Anal.*, vol. 13, pp. 859–870, Dec. 2009.
[18] K. W. Tobin, E. Chaum, V. P. Govindasamy, and T. P. Karnowski, "Detection of anatomic structures in human retinal imagery," *IEEE Trans. Med. Imag.*, vol. 26, no. 12, pp. 1729–1739, Dec. 2007.
[19] A. Hoover and M. Goldbaum, "Locating the optic nerve in a retinal image using the fuzzy convergence of the blood vessels," *IEEE Trans. Med. Imag.*, vol. 22, no. 8, pp. 951–958, Aug. 2003.
[20] M. Foracchia, E. Grisan, and A. Ruggeri, "Detection of optic disc in retinal images by means of a geometrical model of vessel structure," *IEEE Trans. Med. Imag.*, vol. 23, no. 10, pp. 1189–1195, Oct. 2004.
[21] F. Mendels, C. heneghan, and J. P. Thiran, "Identification of the optic disk boundary in retinal images using active contours," in *Irish Mach. Vision Image Process. Conf.*, 1999, pp. 103–115.
[22] J. Lowell, A. Hunter, D. Steel, A. Basu, R. Ryder, E. Fletcher, and L. Kennedy, "Optic nerve head segmentation," *IEEE Trans. Med. Imag.*, vol. 23, no. 2, pp. 256–264, Feb. 2004.
[23] H. Q. Li and O. Chutatape, "Automated feature extraction in color retinal images by a model based approach," *IEEE Trans. Biomed. Eng.*, vol. 51, no. 2, pp. 246–254, Feb. 2004.
[24] J. Xu, O. Chutatape, E. Sung, C. Zheng, and P. C. T. Kuan, "Optic disk feature extraction via modified deformable model technique for glaucoma analysis," *Pattern Recog.*, vol. 40, pp. 2063–2076, Jul. 2007.
[25] T. F. Chan and L. A. Vese, "Active contours without edges," *IEEE Trans. Image Process.*, vol. 10, no. 2, pp. 266–277, Feb. 2001.
[26] A. Aquino, M. E. Gegundez-Arias, and D. Marin, "Detecting the optic disc boundary in digital fundus images using morphological, edge detection, and feature extraction techniques," *IEEE Trans. Med. Imag.*, vol. 29, no. 11, pp. 1860–1869, Nov. 2010.
[27] R. Chrástek, M. Wolf, K. Donath, G. Michelson, and H. Niemann, "Optic disc segmentation in retinal images," *Bildverarbeitung für die Medizin*, pp. 263–266, 2002.
[28] [Online]. Available: http://www.optos.com/en-us/Professionals/Optometry/Case-Clinical-Studies/
[29] L. D. Hubbard, R. J. Brothers, W. N. King, L. X. Clegg, R. Klein, L. S. Cooper, A. R. Sharrett, M. D. Davis, and J. W. Cai, "Methods for evaluation of retinal microvascular abnormalities associated with hypertension/sclerosis in the atherosclerosis risk in communities study," *Ophthalmology*, vol. 106, pp. 2269–2280, Dec. 1999.
[30] S. Chaudhuri, S. Chatterjee, N. Katz, M. Nelson, and M. Goldbaum, "Detection of blood-vessels in retinal images using two-dimensional matched-filters," *IEEE Trans. Med. Imag.*, vol. 8, no. 3, pp. 263–269, Sep. 1989.
[31] D. J. Cunningham, *Cunningham's Text-Book of Anatomy*. New York: Oxford Univ. Press, 1981.
[32] Y. Zhang, B. J. Matuszewski, L.-K. Shark, and C. J. Moore, "Medical image segmentation using new hybrid level-set method," in *Proc. 5th Int. Conf. BioMed. Visualization: Inf. Visualization Med. Biomed. Informatics*, 2008, pp. 71–76.
[33] S. Osher and J. A. Sethian, "Fronts propagating with curvature-dependent speed: Algorithm based on Hamilton-Jacobi formulations," *J. Comput. Phys.*, vol. 79, pp. 12–49, 1988.
[34] H. Yu, M. S. Pattichis, C. Agurto, and M. B. Goens, "A 3D freehand ultrasound system for multi-view reconstructions from sparse 2D scanning planes," *BioMed. Eng. OnLine*, 10:7, 2011.
[35] C. Xu and J. L. Prince, "Snakes, shapes, and gradient vector flow," *IEEE Trans. Image Process.*, vol. 7, no. 3, pp. 359–369, Mar. 1998.
[36] J. Weickert, B. M. H. Romeny, and M. A. Viergever, "Efficient and reliable schemes for nonlinear diffusion filtering," *IEEE Trans. Image Process.*, vol. 7, no. 3, pp. 398–410, Mar. 1998.
[37] H. Yu, S. Barriga, C. Agurto, S. Echegaray, M. Pattichis, G. Zamora, W. Bauman, and P. Soliz, "Fast localization of optic disc and fovea in retinal images for eye disease screening," *SPIE Med. Imag.*, vol. 7963, pp. 17-1–17-12, 2011.
[38] S. Silva, J. Madeira, J., B. S. Santos, and C. Ferreira, "Inter-observer variability assessment of a left ventricle segmentation tool applied to 4D MDCT images of the heart," in *Proc. 33rd Annu. Int. Conf. IEEE Eng. Med. Biol. Soc.*, 2011, pp. 3411–3414, J..
[39] S. Vanbelle and A. Albert, "Agreement between an isolated rater and a group of raters," *Stat. Neerlandica*, vol. 63, no. 1, pp. 82–100, 2009.
[40] B. Efron and R. J. Tibshirani, *An Introduction to the Bootstrap*. London, U.K: Chapman & Hall, 1993.
[41] V. Chalana and Y. Kim, "A methodology for evaluation of boundary detection algorithms on medical images," *IEEE Trans. Med. Imag.*, vol. 16, no. 5, pp. 642–652, Oct. 1997.

Authors' photographs and biographies not available at the time of publication.